Effects of double orifice spacing on bubble behaviors and hydrodynamics in gas-liquid-solid systems through VOF-DEM method

Haozhe Zhang, Na Zhao, Xiaotong Luo, and Jingtao Wang*
School of Chemical Engineering and Technology, Tianjin University, Tianjin 300072, People's Republic of China

(Received 18 November 2021; accepted 1 February 2022; published 22 February 2022)

In this paper, a three-dimensional calculation of the formation and rising of double bubbles in a gas-liquid-solid flow system with two air-intake orifices is done through computational fluid dynamics. The coupled method of volume of fluid (VOF) and discrete element model (DEM) is used to capture the interface of bubbles and track the movement of particles. The numerical method is validated by comparing our numerical results to experimental data (from other literature) of the double-bubble rising process under the same conditions. Two cases of the bubble formation and rising, when particles are laid at the container bottom (case I) and when particles are settling freely (case II), are studied carefully. At first, for case I, the detachment time of the first bubble when there is a proper time difference of the air intake start of two orifices is less than that when the start time is the same. Secondly, for case I, the possible reason of the coalescence of two parallel bubbles and reason of the shift of the bubble queues to the left or right are discussed by analyzing the velocity vector diagrams. By comparing case I and case II, it is disclosed that the free settlement of particles could prevent bubbles from coalescence and weaken the deviation of the bubble queues. Finally, for case II, the suitable distance between two orifices for better particle entrainment under different air intaking velocities is also studied, and it will increase as the air intaking velocity increases. The results of this paper is helpful to the deep understanding of the gas-liquid-solid fluidized system.

DOI: 10.1103/PhysRevFluids.7.024303

I. INTRODUCTION

Multiphase flows refer to flow systems with clear interfaces of two or more phases [1]. The gas-liquid-solid (g-l-s) flow system is one typical flow of the three-phase flow systems, which has large heat transfer areas and good mass transfer efficiency among phases [2–4]. It has been widely used in chemistry, petroleum, energy, environment, food, life, and other industry fields. Flow behaviors of the g-l-s three-phase flow are complicated due to the complex interactions among phases. Thus, many works have been done to study the complex hydrodynamics of g-l-s multiphase flows [5–18].

Both experimental and numerical methods have been employed to investigate the g-l-s multiphase flows [6,7]. As for the numerical methods, they mainly include Eulerian-Eulerian (E-E), Eulerian-Lagrangian (E-L), and direct numerical simulation (DNS) methods. In E-E method, different phases are regarded as the interpenetrating continuous phase medium. The flow velocity and volume fraction of each phase are different based on the volume-average theory. Panneerselvam *et al.* used a multifluid model to calculate the local hydrodynamic properties of gas-liquid-solid three-phase flow systems and compared their results to the experimental data from the paper done by Kiared and Yu. The calculated flow field is in good agreement with the experimental

*wjingtao928@tju.edu.cn

results [9–12]. Compared to E-E method, E-L method solves Navier-Stokes equations in Eulerian coordinate system for the continuous phase, and solves the particle orbit equations for particles and other discrete phases in Lagrangian coordinate system. Based on E-L method, Delnoij *et al.* studied a gas-liquid two-phase bubble tower, and calculated the bubble coalescence, trajectory and wake vortex [13]. Zhang *et al.* established an E-E-L model for gas-liquid-solid three-phase slurry reactors. In this model, the liquid phase was solved by a governing equation based on the volume-average method, while the movement of bubbles and particles were solved by Lagrangian trajectory analysis method [15]. The discrete element model (DEM) used in this paper is a typical E-L method, which used Lagrangian method to track the trajectory of a single particle [16]. DEM method could calculate the interaction among individual particles in details, and could observe the stacked structure of particle swarms and track the rearrangement of particles. Combining DEM with computational fluid dynamics (CFD) to solve the complex particle-flow problems is very popular at this stage [17]. Namdarkedenji *et al.* used CFD-DEM method to study the effect of the uniform flow and pulsed flow on the fluidization of gas-solid fluidized beds, which is useful to guide the industrial application [18].

Among g-l-s multiphase flows, the formation and rising of bubbles have an important impact on the hydrodynamics of the flow systems. Thus, the study and analysis of bubble formation processes, bubble shapes, bubble rising speeds, bubble coalescence, and bursting are of great significance to the in-depth understanding of the interaction between different phases, especially for the interaction between fluid and particle phases [5]. Nowadays, there are a variety of numerical models which could be used to capture the gas-liquid interface of two-phase flows in fluidized beds, and volume of fluid (VOF) method is the most popular [19]. Based on VOF method, Zhang *et al.* developed a computational model for g-l-s three-phase slurry reactors. When Reynolds number is low, it could be observed that one bubble has two symmetrical closed wake vortices; in the case of high Reynolds number, the unstable periodic asymmetric wake vortex could be observed [20]. Xu *et al.* combined a discrete phase method (DPM) with CFD-VOF and used this CFD-VOF-DPM method to investigate the bubble formation through a single air orifice in the g-l-s fluidization system with particles of low holdup. They discussed the effects of particle and fluid properties on the bubble behaviors systematically [21].

Hydrodynamics of bubble rising is an important subject in the mechanics of multiphase flows [22,23]. Recently, there are many experimental studies on the speed, shape, trajectory, and coalescence of rising bubbles. Based on Kirchhoff's equations and physical parameters obtained from experiments, Shew *et al.* [24] proposed a model composed of four ordinary differential equations to simulate the rising process of a bubble. According to this model, the zigzag and spiral rising trajectories of the bubble in water are caused by the instability of wake. Wang *et al.* [25] presented that the shape and speed of a rising bubble would change with Reynolds numbers during the rising process. They also disclosed a critical Reynolds number (Re*): when $\mathrm{Re} > \mathrm{Re}*$, the bubble accelerated continuously in the fluid; when $\mathrm{Re} < \mathrm{Re}*$, the bubble moved with a constant speed after accelerating to a certain speed. Huang *et al.* [26] observed and compared the formation and rising process of two parallel bubbles for different orifice sizes and distances. The result shows that the distance between two bubbles would change when two parallel bubbles were rising side by side. When the orifice sizes and gas flow rates were the same, the smaller the orifice distance was, the smaller the size of the first bubble, and the smaller the final stable velocity; when the orifice distances and gas flow rates were the same, the larger the orifice size was, the larger the size of the first bubble, and the larger the final stable velocity.

In addition, numerical simulation has also been used to study the hydrodynamics of the bubble rising. Up to now, some researchers have used VOF model to investigate the interaction between bubbles formed through double orifices and multiple orifices in gas-liquid flow systems. Zhang *et al.* [27] studied the formation, growth, detachment, and rising of bubbles through orifices of different numbers (one, two, and four) in bubble columns. They analyzed the interaction between two parallel bubbles and presented that the coalescence would occur when the distance between orifices is closer. VOF-DPM model was also used by some researchers to study behaviors of two

parallel bubbles in 3D gas-liquid-solid flow systems. The method combining VOF with DEM could capture the phase interface effectively when simulating the complex particles flows. Wu *et al.* [28] applied VOF-DEM method to study the free surface flow with particles in a stirred tank. Zhao *et al.* [29] used the same VOF-DEM method to study the formation and rising of a bubble in a gas-liquid-solid system. They reported that the detachment time of the first bubble is longer when particles are at the container bottom than that when the particles are settling freely. The sedimentation of particles induced a stronger circulation near the container bottom, and enhanced the bubble detachment. Up to now, according to our best knowledge, nobody has used VOF-DEM method to explore the interaction between two or more bubbles during the bubble rising process.

Based on the same VOF-DEM method of Zhao *et al.*, this paper calculates the hydrodynamic behaviors of double rising bubbles in a gas-liquid-solid flow system. This coupled method considers the particle collisions and the effect of particle volumes on the continuous phase which are neglected by DPM model. This paper mainly investigates the merging possibility of two rising bubbles and the particle entrainment of bubbles when the orifice distance is changed, and the effects of operation conditions are also discussed systematically. In Sec. II, the mathematical model is presented in detail. In the third section, the numerical model is verified through several examples. The calculated results are presented and discussed in Sec. IV. Finally, the conclusion is given in Sec. V.

II. MODEL DESCRIPTION

A. VOF method

Volume of fluid method is based on the momentum conservation equation and the fluid volume fraction equation, which could track the phase interface by solving the continuity equation of the volume fraction of one or more phases. Different fluids share the same set of momentum equations, and in order to track the phase interface, the phase volume fraction "φ" is introduced to represent the volume fraction occupied by the main phase in each calculation unit. The dynamic behavior of the phase interface is given by the continuity equation

$$\frac{\partial \varphi}{\partial t} + u_f \cdot \nabla \varphi = 0. \tag{1}$$

The detailed description of this equation was given in our previous paper [28,29].

The motion of the fluid phase is calculated through the volume-averaged governing equations. The mass conservation equation (continuity equation) and the momentum conservation equation are [30]

$$\frac{\partial (\varepsilon_f \rho_f)}{\partial t} + \nabla \cdot (\varepsilon_f \rho_f \mathbf{u}_f) = 0, \tag{2}$$

$$\frac{\partial (\varepsilon_f \rho_f \mathbf{u}_f)}{\partial t} + \nabla \cdot (\varepsilon_f \rho_f \mathbf{u}_f \mathbf{u}_f) = \varepsilon_f (-\nabla p + \nabla \cdot \boldsymbol{\tau} + \rho_f \mathbf{g} + \mathbf{f}_s) + \mathbf{f}_{pf}, \tag{3}$$

where ε_f, ρ_f, and $\mathbf{u}_f$ are grid void fraction, fluid density, and fluid velocity, respectively. In addition, $\boldsymbol{\tau}$ is the viscous stress tensor. $\mathbf{f}_{pf}$ is the momentum exchange term between the fluid and the particle, and $\mathbf{f}_s$ is the surface tension, which is calculated by continuum surface force (CSF) model [31].

B. DEM method

Solid particles generally have two types of movement, translation and rotation. In DEM method, they could be described according to Newton's second law and the angular momentum equation

[32]:

$$m_i \frac{d\mathbf{v}_i}{dt} = \mathbf{F}_{c,i} + \mathbf{F}_{p,i} + \mathbf{F}_{f,i} + m_i \boldsymbol{g}, \tag{4}$$

$$I_i \frac{d\mathbf{w}_i}{dt} = \sum_{j=1, i\neq \mathrm{j}}^{N} (\mathbf{T}_{t,ij} + \mathbf{T}_{r,ij}), \tag{5}$$

where m_i and I_i are the mass and the inertia moment of the ith particle; $\mathbf{v}_i$ and $\mathbf{w}_i$ are the translation and angular velocities of particle i; $\mathbf{F}_{c,i}$, $\mathbf{F}_{p,i}$, and $\mathbf{F}_{f,i}$ are the contact force, pressure gradient force, and particle-fluid interaction force on particle i, respectively; $\mathbf{T}_{t,ij}$ and $\mathbf{T}_{r,ij}$ represent the tangential and rolling friction torque between particle i and particle j, respectively; N represents the total number of particles in the system.

Details of these two equations in DEM method have been mentioned in the previous paper of our group [28,29]. The force between solids is divided into the interaction force between the particles and the interaction force between the particles and the wall. $\mathbf{F}_{c,i}$ could be split into the normal force and tangential force [16], which are calculated by Tsuji model [33] and Mindlin model [34], respectively.

C. Particle-fluid interaction

In VOF-DEM method, the interaction between particles and fluids must be considered, for example, the drag force $\mathbf{F}_{d,i}$, pressure gradient $\mathbf{F}_{\nabla p,i}$, viscous stress $\mathbf{F}_{\nabla\cdot\tau,i}$, capillary force $\mathbf{F}_{s,i}$, virual mass force $\mathbf{F}_{vm,i}$, Bassett force $\mathbf{F}_{B,i}$, Saffman lift $\mathbf{F}_{\mathrm{saff},i}$, and Magnus lift $\mathbf{F}_{\mathrm{Mag},i}$. The total particle-fluid interaction force is calculated by the following expression:

$$\mathbf{F}_{pf,i} = \mathbf{F}_{d,i} + \mathbf{F}_{\nabla\cdot\tau,i} + \mathbf{F}_{\nabla p,i}, + \mathbf{F}_{s,i} + \mathbf{F}_{vm,i} + \mathbf{F}_{B,i} + \mathbf{F}_{\mathrm{Saff},i} + \mathbf{F}_{\mathrm{Mag},i}. \tag{6}$$

The drag force is the most important, and its expression is

$$\mathbf{F}_{d,i} = \frac{\beta V_i}{1-\varepsilon_f}(\mathbf{u}_f - \mathbf{v}), \tag{7}$$

where $\mathrm{V_i}$ is the volume of the particle, and β is the interphase momentum transfer coefficient. It is crucial to the correctness of the calculation result and is calculated by Ergun and Wen and Yu model modified by Gidaspow [35]:

$$\beta = \begin{cases} 150\frac{(1-\varepsilon_f)^2}{\varepsilon_f}\frac{\mu_f}{{d_p}^2} + 1.75(1-\varepsilon_f)\frac{\rho_f}{d_p}|\mathbf{u}_f - \mathbf{v}| & \varepsilon_f \leqslant 0.8 \\ \frac{3}{4}C_D\frac{\varepsilon_f(1-\varepsilon_f)}{d_p}\rho_f{\varepsilon_f}^{-2.65}|\mathbf{u}_f - \mathbf{v}| & \varepsilon_f > 0.8 \end{cases}, \tag{8}$$

where d_p is the diameter of the solid particle, C_D is the drag coefficient, and $\mathrm{Re_p}$ is the particle Reynolds number. C_D and $\mathrm{Re_p}$ are calculated by the following two equations, respectively:

$$C_D = \begin{cases} \frac{24}{\mathrm{Re}_p}\left(1 + 0.15{\mathrm{Re}_p}^{0.687}\right) & \mathrm{Re}_p \leqslant 1000 \\ 0.44 & \mathrm{Re}_p > 1000 \end{cases}, \tag{9}$$

$$\mathrm{Re}_p = \frac{\varepsilon_f \rho_f d_p |\mathbf{u}_f - \mathbf{v}|}{\mu_f}. \tag{10}$$

D. Coupling strategy

VOF-DEM model used in this paper is based on commercial softwares ANSYS FLUENT and EDEM. At the beginning of the calculation, FLUENT calls a user-defined initialization function to obtain the position of particles. When the grid void ratio is calculated through the virtual double-grid model, the fluid-particle interaction force is calculated. Then, EDEM starts the calculation task at the

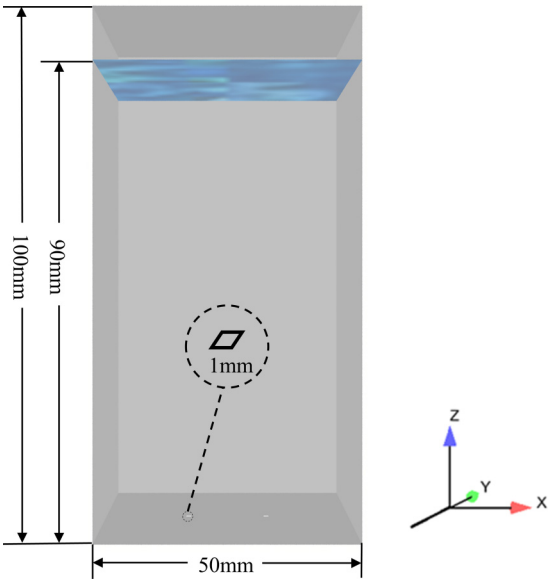

FIG. 1. Geometric structure of the gas-liquid-solid flow system.

first time step, and updates the velocity and position of the particles by solving Newton's second law and the angular momentum equation after obtaining the fluid-particle interaction force. Based on the updated particle information, the grid void ratio and the fluid-particle interaction force are recalculated. After this step is completed, EDEM would return the calculation to FLUENT. FLUENT will use the updated fluid-particle force to start the iterative calculation of the continuity equation and the governing equation. The entire calculation control is handed over to EDEM, and the fluid-particle interaction force is recalculated based on the converged calculation results of the flow field, and the next calculation cycle is started [28].

E. Simulation conditions

In this paper, a cuboid container with dimensions of $50 \times 50 \times 100\,\mathrm{mm}^3$ is used for the calculation of the bubble formation in g-l-s flow systems (see Fig. 1). Around the center of the container bottom, there are two square orifices with an edge of 1 mm. The distance between two orifices is changed for different calculation cases. The top of the container is open to the atmosphere, and the four walls are all set to no-slip boundary conditions. The gas-liquid interface is set 10 mm away from the top edge and divides the flow system into the lower liquid zone and the upper gas zone. The particles are randomly generated in the liquid phase and settle freely to the bottom. At the beginning of the calculation, air is injected into the flow system through the orifices, and the entire system is a gas-liquid-solid three-phase flow system. Table I lists the physical properties of the fluids and particles, and Table II lists the values of the model parameters.

TABLE I. Physical properties of the fluids and particles.

ρ_l (kg m^3)	μ_l (Pa s)	ρ_g (kg m^3)	μ_g (Pa s)	σ (N m)	d_p (mm)	ρ_p (kg m^3)
1000	0.001	1.225	1.78×10^{-5}	0.073	0.4	2500

TABLE II. Values of model parameters in the simulation.

Parameter	Value
Particle Poisson's ratio	0.25
Particle shear modulus	1×10^6 Pa
Coefficient of restitution	0.5
Coefficient of static friction	0.5
Coefficient of rolling friction	0.01
CFD time step	1×10^{-4} s
DEM time step	1×10^{-5} s

III. MODEL VERIFICATION

In this section, the suitable grid size for the above geometric model is selected through the verification of grid independence. Then, two kinds of ways are employed to verify the accuracy and validation of the model. (1) The particle swarm entering the water is simulated to verify the volume conservation. (2) Verifying the model by comparing to the experimental data from other literature. Generally, single-particle sedimentation is used to verify the accuracy of the coupling process of VOF-DEM and particle-fluid interaction [36,37]. However, the coupling method employed in this paper is exactly the same as the one in our previous paper, and the check of the single-particle sedimentation has been done in that paper [29]. Thus, we would not repeat this check in this paper.

A. Grid independence verification

The instantaneous velocity of rising bubbles with an air-taking velocity of 0.5 mm/s in the water is calculated under different grid sizes in order to verify the grid independence. Five different grid sizes are selected: 0.30, 0.50, 0.75, 1.00, and 1.25 mm. Except for the first bubble, the bubble at the height of 25 mm is also selected in order to validate smaller bubbles. The calculated results are shown in Fig. 2. Assuming the result for the smallest grid size (0.30 mm) is the accurate one, it could be seen from Fig. 2 that the error is obviously increased when the grid size is raised from 0.50 to 1.25 mm. When the grid size is 0.50 mm, the calculated result is very close to the one for 0.30 mm, and the error is quite small. Considering the demand of both the calculation accuracy and cost, the grid size of 0.5 mm is selected to do the following simulation.

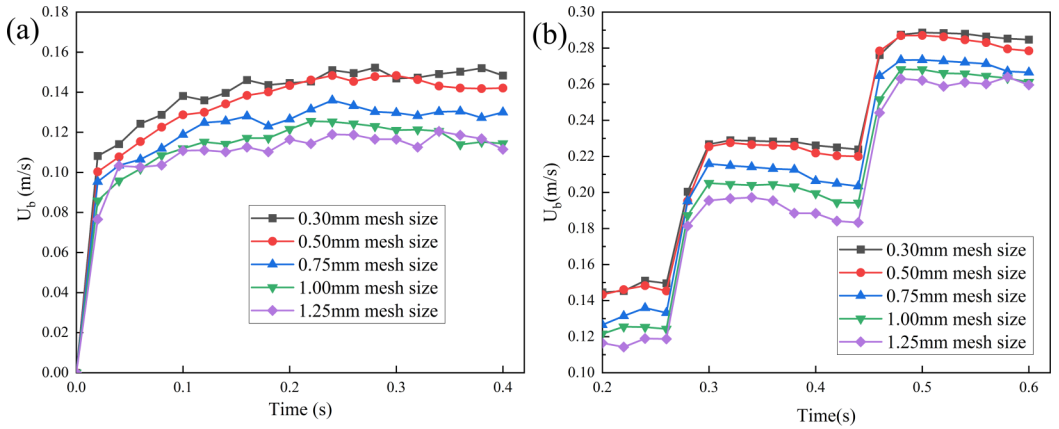

FIG. 2. The instantaneous velocity U_b of the first bubble (a) and the bubble at the height of 25 mm (b) rising in the water for different grid sizes.

TABLE III. Parameter employed for the simulation shown in Fig. 3.

ρ_l (kg m^3)	μ_l (Pa s)	ρ_g (kg m^3)	μ_g (Pa s)	d_p (mm)	ρ_p (kg m^3)
1000	0.001	1.225	10^{-5}	2.0	2500

B. Water entry of a particle swarm

The problem of the volume conservation of particle swarms entering water is a classic problem in the field of computational fluid dynamics, and it has been successfully realized by some researchers [38,39]. The sedimentation of the particle group involves the collisions among particles. Thus, it is much more complicated than the sedimentation of a single particle. The correctness of VOF-DEM model used in this paper is further verified through the volume exchange between the particle swarm and the water phase. It is well known that particles would occupy part of the volume of the water and cause the rise of the liquid surface when the particle swarm enters water. The rise height of the liquid surface is equal to the quotient of the total volume of particles entering water divided by the cross-sectional area of the container.

In this simulation, the dimension of the calculation domain is 50 mm × 50 mm × 200 mm, the gravitational acceleration is in the $-z$ direction, and its value is 9.81 m/s^2. All boundary conditions are set as the non-slip boundary conditions, and the top is open to the atmosphere. The entire domain uses a uniform grid size of 0.4 mm, and the initial height of the water surface is $z = 50$ mm. The calculation domain is divided into the air zone and water zone. The parameters used in the simulation are shown in Table III. A total of 9600 particles are placed in a cell of 20 × 20 × 24, the initial position is just on the water surface, and the initial distance between the two adjacent particles is 0.20 mm. The Poisson ratio of the particles is 0.25, the shear modulus is 107 Pa, the coefficient of restitution is 0.5, the coefficient of static friction is 0.5, and the coefficient of rolling friction is 0.01.

It could be seen from Fig. 3 that the process of particles falling from the air into the water causes a significant rise of the water surface. The height of the water surface at $t = 0.0$ s is 50 mm. All the particles settle down when $t = 2.0$ s, and the position of the water surface is at $z = 66.070$ mm. This means that the calculated value of the surface rise caused by all the sinking particles is 16.070 mm when VOF-DEM model is employed in this paper. It is very close to the theoretical value of

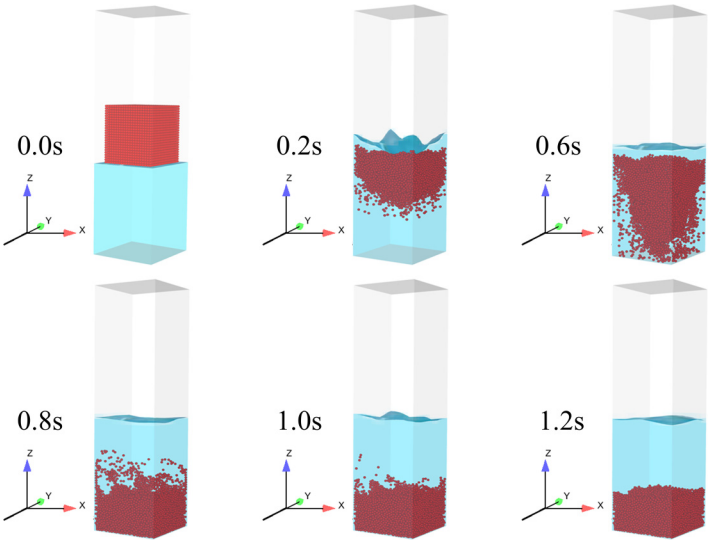

FIG. 3. Snapshots of the particle swarm falling into water.

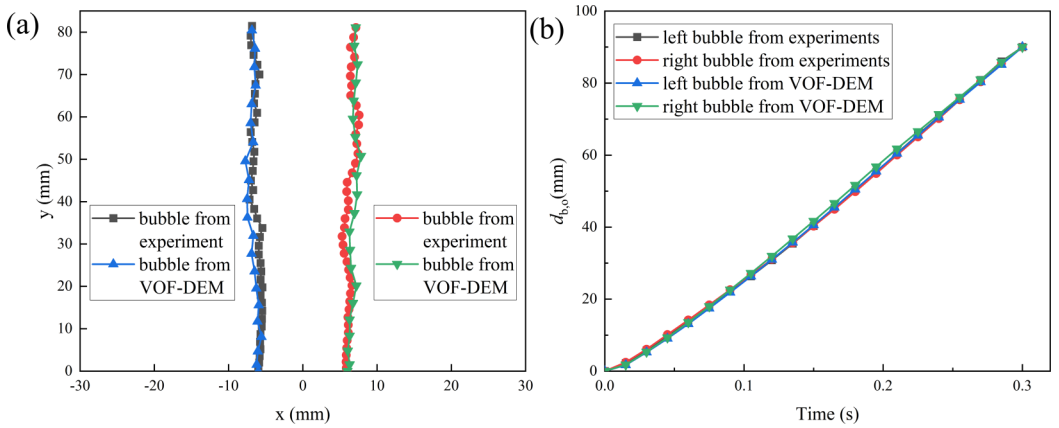

FIG. 4. Comparison of bubble rising trajectory (a) and the distance between the bubble and corresponding orifice (b) in simulation and experiment.

16.085 mm ($\Delta h = 9600 \times \frac{\pi}{6}(0.002)^3/(0.05)^2$), and the relative error is only 0.093%. This fully verifies the excellent volume conservation of VOF-DEM model when calculating a three-phase flow system.

C. Validation through comparison to experiments

In order to validate VOF-DEM model, we compare the calculated results to Huang's experimental data [26]. The physical parameters from Huang's experiment are taken in the numerical calculation. The geometry of the calculated system is a cubic water tank of 300 mm × 300 mm × 500 mm, and there are two circular orifices with a 1.5 mm diameter at the container bottom. In addition, the intaking velocity of the air is fixed to 2.0 m/s. The rising trajectories of bubbles from experiment and calculation are compared in Fig. 4(a), and the left and right deviation of the rising bubbles are almost negligible comparing to the rising height. Therefore, the curve of the distance between bubble and its orifice ($d_{b,o}$) over time is obtained to calculate the relative error ($\delta_1 = 0.934\%$ and $\delta_2 = 1.217\%$) in Fig. 4(b). It could be seen that the calculation results are in good agreement with the experimental data.

IV. RESULTS AND DISCUSSION

A. Hydrodynamics when particles are laying at the bottom

1. Coalescence for different orifice distances

According to the work of Zhao *et al.* [29], the generation of the first bubble in a g-l-s system has three stages: expansion, contraction, and detachment. Then, during the rising process, the wake of the first bubble affects the subsequent bubbles through strong shear forces. Thus, subsequent bubbles could detach from the orifice more easily, and they are smaller and faster than the first bubble. The subsequent bubbles would catch up with the first bubbles and merge with it. Thus, the first bubble is largest; the size of the subsequent bubbles are almost the same after the flow system is stable. Therefore, it is necessary to measure the diameter of the first bubble during its formation and rising process before studying the effects of different orifice spacing on the coalescence of two parallel bubbles. As shown in the paper of Zhao *et al.*, the diameter of the first bubble is about 6.5 mm at the moment before its detachment, and about 8.6 mm when it touches the gas-liquid interface at the top of the container [29]. According to these results, under the same conditions, when the distance between two orifices is less than 6.5 mm, the two first bubbles would coalesce during the expansion stage at the container bottom; when the distance of two orifices is between 6.5 and 8.6 mm, the two

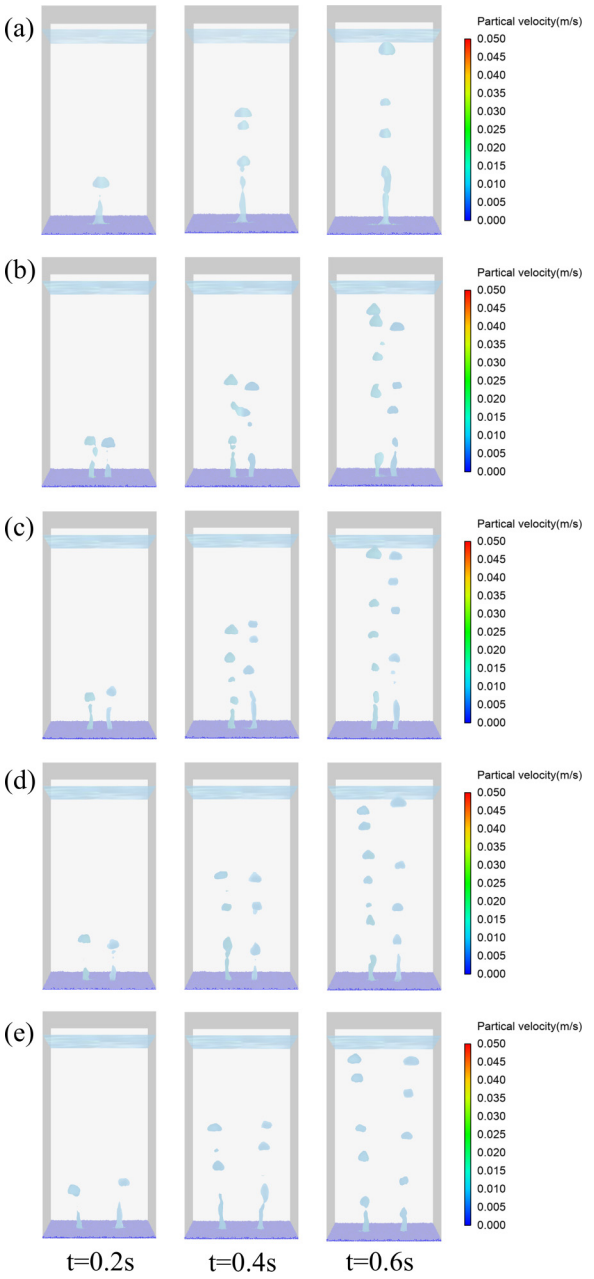

FIG. 5. The formation and rising of double bubbles for different distances (d_s) between orifices when particles are laying at bottom. (a) $d_s = 6$, (b) $d_s = 8$, (c) $d_s = 10$, (d) $d_s = 12$, and (e) $d_s = 18$ mm.

first bubbles would coalesce during the rising process. Considering the influence of the wake caused by the first bubble on the behaviors of subsequent bubbles, five cases with the orifice spacing of 6, 8, 10, 12, and 18 mm are selected to study the effects of different spacing on the bubble behaviors. In this section, the velocity of the air is fixed to 0.5 m/s.

The calculation results are shown in Fig. 5. When the distance between two orifices is 6 mm, the two first bubbles merge with each other during the formation process, and the rising process is

almost the same as that of a single bubble. For the case with the orifice spacing of 8 mm, the two first bubbles do not coalesce during the rising process, but the two second bubbles from different orifices coalesce during the rising process. The trajectories of bubbles for the orifice spacing of 10 and 12 mm are not straight vertical lines during the rising, but incline towards the container wall a little. While for the case with the orifice spacing of 18 mm, the deviation of the rising trajectory from the vertical line is so obvious that it seems that the two bubbles are attracted by the wall. The reasons for these phenomena will be discussed through velocity vector diagrams in the following.

According to Fig. 5, there are three types of bubble coalescence for the formation and rising of double bubbles: bubble coalescence inside a single queue of bubbles (BCSQ), coalescence of two bubbles belonging to different queues during the bubble formation (BCDQF), and coalescence of two bubbles belonging to different queues during the bubble rising (BCDQR). BCSQ is common during the bubble-rising process, because the first bubble is the largest and the slowest, and thus, is easier to be caught up and merged with the subsequent bubbles. This kind of coalescence has been discussed in the literature [29] for the formation and rising of a single bubble. BCDQF is the coalescence occurring at the expansion stage of the formation of the two first bubbles due to the orifice distance is less than the maximum diameter of the two first bubbles. In this paper, BCDQR will be discussed mainly.

BCDQR is the coalescence occurring between two bubbles from two different queues during the rising process when the distance between two orifices is small enough [see Figs. 5(b) and 6(a)]. When the orifice distance is large, the two queues of bubbles could not merge, but shift upwards separately, and the trajectory is not strictly vertical, but inclined towards the wall [see Fig. 5(e)]. These phenomena could be explained by analyzing the velocity vectors in the xz plane of the container [see Figs. 6(b) and 6(d)]. Figure 6(b) shows velocity vector diagrams from time 0.37 to 0.45 s for the orifice distance of 8 mm, and Fig. 6(d) shows those from 0.45 to 0.53 s for $d_s = 18$ mm. According to Fig. 6(b), when the orifice distance is small, the vector arrows of the two queues of bubbles are all pointing upwards and almost merge to one big zone. Due to the rising of the two first bubbles, the water around the two bubbles is pushed away obliquely upward. When the water reaches the container wall, one part moves downwards along the wall to fill the empty space due to the rising of bubbles and ensure the volume conservation. When these water streams are close to the container bottom, they turn around, move towards the container center, and finally move upwards together with the bubble queues. Thus, two big vortices are generated on the two sides of the bubble queues. Under the action of the vortex currents, the two queues of bubbles are pushed towards each other, and some subsequent bubbles collide and merge. However, when the orifice distance is big enough, the situation is different. Due to the interval between the two first bubbles being too wide, the fluids do not move upwards together with the two rising bubbles [see Fig. 6(d)]. On the contrary, they move downwards just like the water pushed away by the rising bubbles along the wall. When the fluids between the two bubble queues flow downward, they would be blocked by the upward currents generated by the rising bubbles. The flow fields between two bubble queues are more turbulent than outside, and thus the vortices between bubble queues are smaller and stronger, although outside the two bubble queues, there are still two big vortics near the container wall for this case. The stronger turbulent vortices and eddies between these two bubble queues will cause the left and right deviation of the rising bubbles [sees Figs. 5(e) and 6(c)].

2. Bubble formation and rising for air intakes with different starting time through two orifices

In this section, the study mainly focuses on the bubble formation and rising when the air is injected into the container through two orifices at different starting time. The difference of bubble behaviors between two cases is when the air intakes start simultaneously for the two orifices and when the air-intakes start with a time difference for the two orifices. Here, the distance of two orifices is fixed to 18 mm, and the rest of the parameters are the same as those in the previous section.

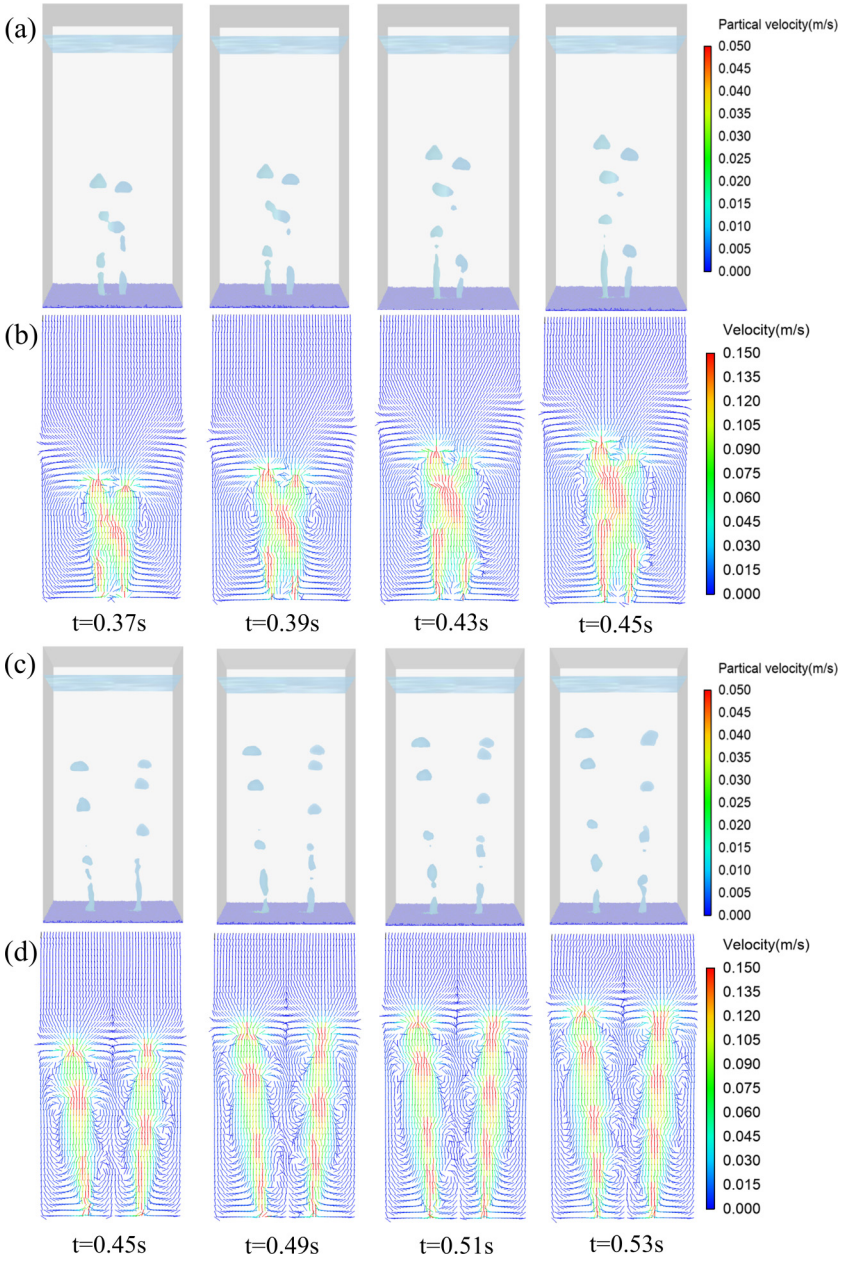

FIG. 6. Details of the bubbles rising and velocity vector diagrams for different distances between orifices when particles are settled at bottom: (a), (b) $d_s = 8$ mm; (c), (d) $d_s = 18$ mm.

As shown in Fig. 7, since the air is injected through the left orifice at the earlier time, the left first bubble is formed and detached from the orifice earlier than the right one. In addition, during the rising process, the left bubble queue is always higher than the right one. Comparing to the case that the air intakes start at the same time for the two orifices, which has a relatively symmetric process of the bubble rising, when the air intakes start with a time difference, the trajectory of the bubble

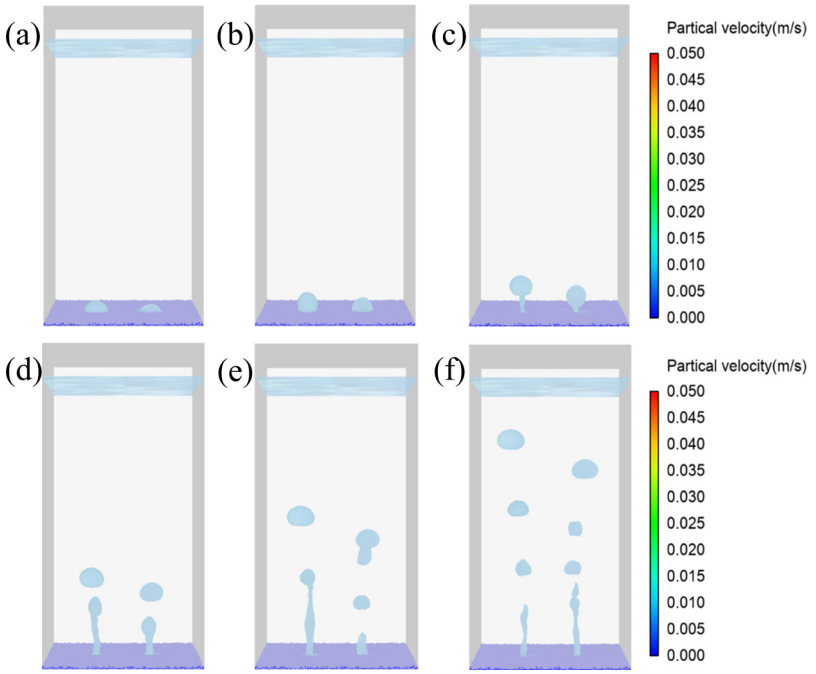

FIG. 7. Calculation results of the formation and rising of two bubble queues when the air intakes start at different time through the two orifices. (a) $t = 0.1$, (b) $t = 0.2$, (c) $t = 0.4$, (d) $t = 0.6$, (e) $t = 0.8$, and (f) $t = 1.0$ s.

rising is not symmetric, but deviates to the left a little. Moreover, the trajectory shown in Fig. 7(f) is not straight, but a little curved, different from the almost straight trajectory shown in Fig. 6(c).

Figure 8 shows the velocity vector diagrams in the xz plane during the rising process of the bubble when the air intakes start at different time. As the left first bubble rises earlier and higher than the right one, more fluids at the left half of the container are pushed moving away towards the top g-l surface. Since the upward flows at the right half start a little later than the left one, part of the left flows enter the right half and move in the upper-right direction, which causes an obvious asymmetric flow field near the top of the two bubble queues. When these currents reach the container wall, half of them move downwards along the wall, and finally form a big vortex on the right side of the right queue. Similarly, on the left side of the left queue, there is also a big vortex. However, as part fluids at the left half enter the right half, the right vortex is stronger than the left one. Thus, the two bubble queues shift a little to the left, and the bubbles no longer move symmetrically during the rising process. Moreover, the trajectories of the bubble queues are not straight, but a little curved, especially for the right queue. Due to the stronger right vortex, it will push the subsequent bubbles at the waist of the right queue to the left; however, the first bubble will move in the upper-right direction due to the currents around it. Thus, the trajectory of the right bubble queue is curved. According to Figs. 8(c) and 8(d), as the left bubble queue is too close to the left side wall, the vortex on the left side of the bubble gets weaker and weaker until it almost cannot be observed.

Figure 9 shows the velocity vector diagrams of the container bottom for the two cases: when the air intakes start simultaneously for the two orifices [see Fig. 9(a), case I] and when the air intakes start with a time difference for the two orifices [see Fig. 9(b), case II]. It is obvious that the flow fields shown in Fig. 9(a) are almost symmetric, while the flow fields shown in Fig. 9(b) are asymmetrical due to the different air-intake time. The left orifice starts to intake air first, and the time difference is 0.1 s. For case I, during the expansion stage of the first bubble, the simultaneous expansions

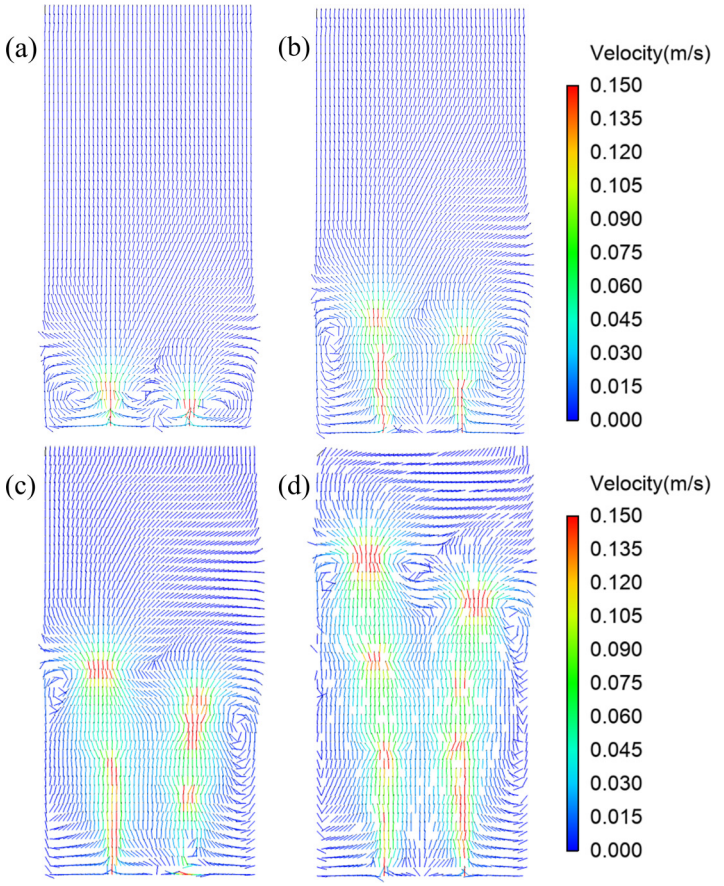

FIG. 8. Velocity vector diagrams during the rising process of two bubble queues when the air intakes start at different time through the two orifices. (a) $t = 0.4$, (b) $t = 0.6$, (c) $t = 0.8$, and (d) $t = 1.0$ s.

of two forming bubbles will increase the pressure at the zone between two orifices, which will hinder the expansion of the two first bubbles. Also, during the contraction stage, the simultaneous contractions of two forming bubbles will cause the pressure decrease between two orifices, which will also hinder the formation of the two first bubbles. However, the situation is different for case II. During the expansion stage of the first bubble, the left first bubble expands, while the right first bubble has not started to expand and could not hinder the expansion of the left bubble. During the contraction stage of the left bubble, the right first bubble is in the expansion stage, which will push its surrounding fluid and particles to move towards the left bubble and enhance the contraction of the left bubble. Thus, the left first bubble could contract and detach faster, and thus, its formation time is relatively less.

B. Hydrodynamics when particles are freely settling

1. Bubble coalescence for different orifice distances

In this section, the study focuses on the bubble rising when the particles are freely settling. Twenty thousand particles are generated randomly in the lower half of the container through the $50 \times 50 \times 50$-mm cubic particle factory. The distance between two orifices is also fixed to 6, 8, 10, 12, and 18 mm, respectively, and the velocity of the air is fixed to 0.5 m/s, the same as that in the previous section.

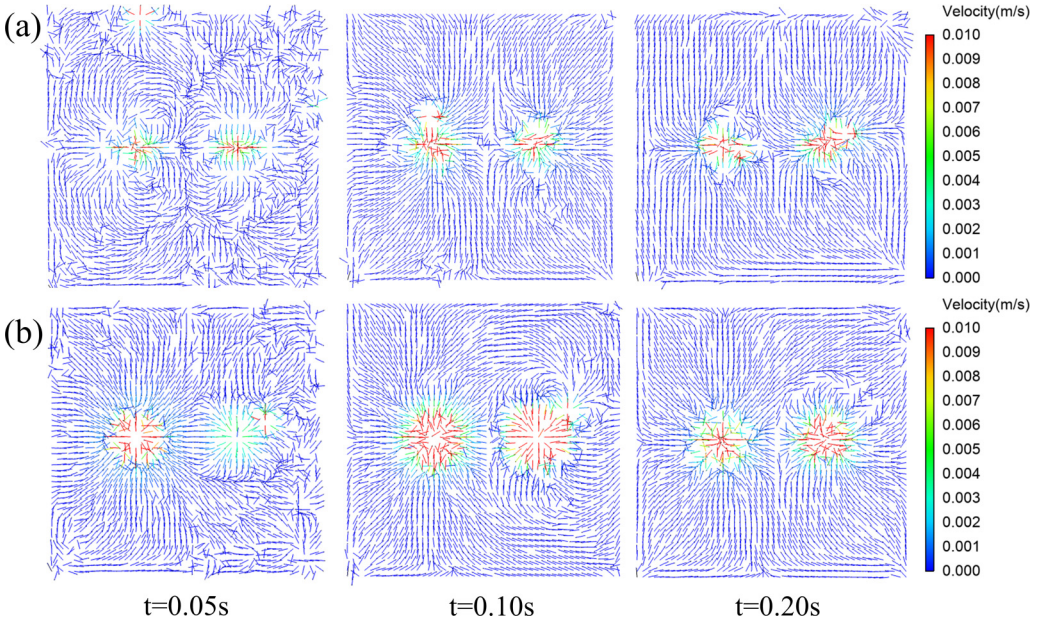

FIG. 9. Velocity vector diagrams of the container bottom for two cases, when the air intakes start simultaneously for the two orifices (a) and when the air intakes start with a time difference for the two orifices (b).

The formation and rising of double bubbles generated through two orifices with different distances when particles are freely settling are shown in Fig. 10. Compared to Fig. 5, the general processes are very similar. However, if observing these pictures more carefully, there are still some differences. The first obvious one is that the coalescence between two bubbles from two different queues does not occur when the orifice distance is 8 mm as shown in Fig. 10(b). Secondly, according to our careful calculation and analysis, the formation and rising speed of bubbles when particles are freely settling are slightly faster than those when particles are laying at the bottom. This is consistent with the results of the formation and rising of a single bubble investigated in our previous paper [29].

When the particles are laying at the bottom (case I), the movement of the water phase is only caused by the rising of the bubbles; however, when the particles are freely settling (case II), as the particles will occupy more spaces at the lower half of the container, the water will be pushed moving upward. Thus, the water movement for case I is relatively a little weaker than that for case II, since the latter is caused by both the bubble rising and the particle settling. As the main movement of the water is in the vertical direction, upwards or downwards, the relatively stronger water currents will enhance the upward movement of the bubbles and hinder the left or right shift of the bubbles, which could be seen in Fig. 11. As shown in Fig. 11(b), the water currents including small vortices between the two bubble queues is obvious, which separate the two queues and hinder the coalescence of bubbles from two queues. It can be clearly seen from the video in the Supplemental Material [40]. This is different in Fig. 6(b); when time is around 0.4 s, the currents of two bubble queues almost merge with each other. According to Fig. 11(d), the clear flow fields show that the two bubble queues move upwards more straightly than those in Fig. 6(d), just shift a little to the left or the right.

2. Particle entrainment for different orifice distances under the fixed air-intaking velocity

Particle entrainment is an important phenomenon during the bubble rising process (see Fig. 10), which is the basis of the gas-liquid-solid fluidized beds [20,41]. The more particles are entrained by the rising bubbles, the easier the solid phase is fluidized in the fluidized bed. An excellent ability

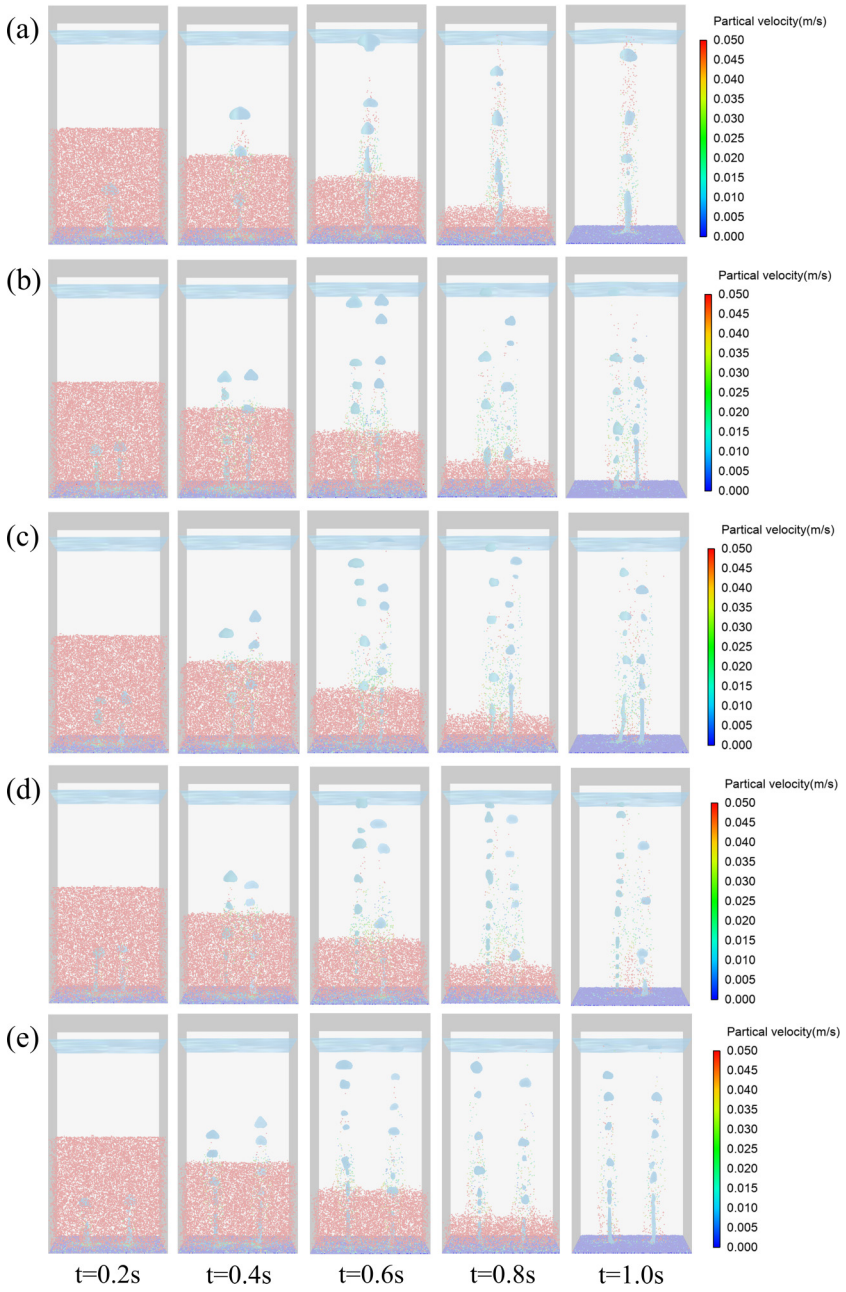

FIG. 10. The formation and rising process of double bubbles with different orifice distance (d_s) when particles are freely settling. (a) $d_s = 6$, (b) $d_s = 8$, (c) $d_s = 10$, (d) $d_s = 12$, and (e) $d_s = 18$ mm.

of the particle entrainment could make the reaction more fully proceed in a fluidization process. Thus, this section discusses the effects of different orifice spacing on the particle entrainment when particles are freely settling, and tries to find the best orifice spacing for a specified air-intaking velocity. In this section, only the particles beyond the top surface of the particle swarm are counted as the entrained particles.

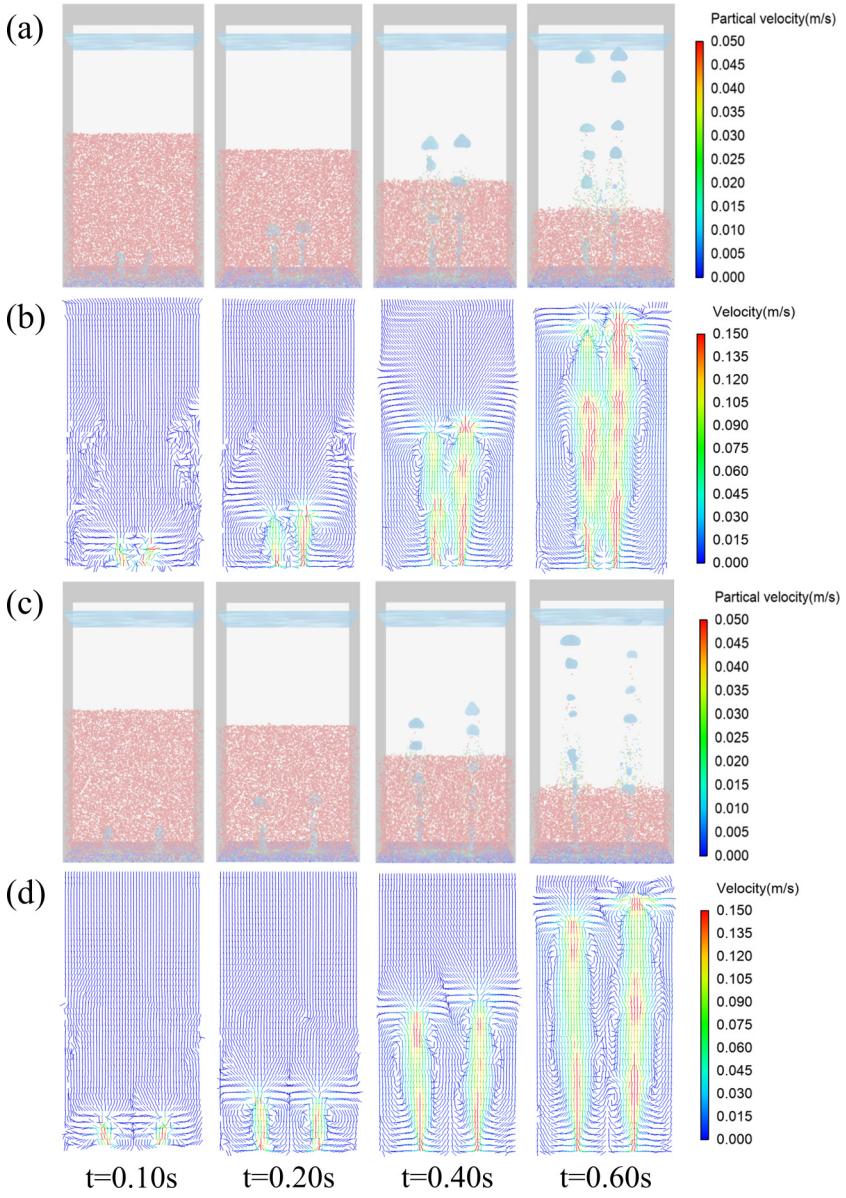

FIG. 11. Details of the bubbles rising and velocity vector diagrams for different distances between orifices when particles are freely settling. (a), (b) $d_s = 8$ mm; (c), (d) $d_s = 18$ mm.

The entire domain is divided into 20 modules in the vertical direction in order to count the particle numbers at different heights. According to the counting results, fitted curves of particle numbers versus height are shown in Fig. 12. It could be seen that the curve for $d_s = 6$ mm is clearly separated from the other four curves. According to Fig. 12, the other four curves interweave with each other and form a curve group different from the last one for $d_s = 6$ mm. For time $t = 0.6$ s [see Fig. 12(a)], when the height is lower, the entrained particles are less for $d_s = 6$ mm; when the height is relatively higher, the entrained particles are more for $d_s = 6$ mm; and when close to the top g-l surface, the entrained particles approach zero for all the orifice distances. These mean that

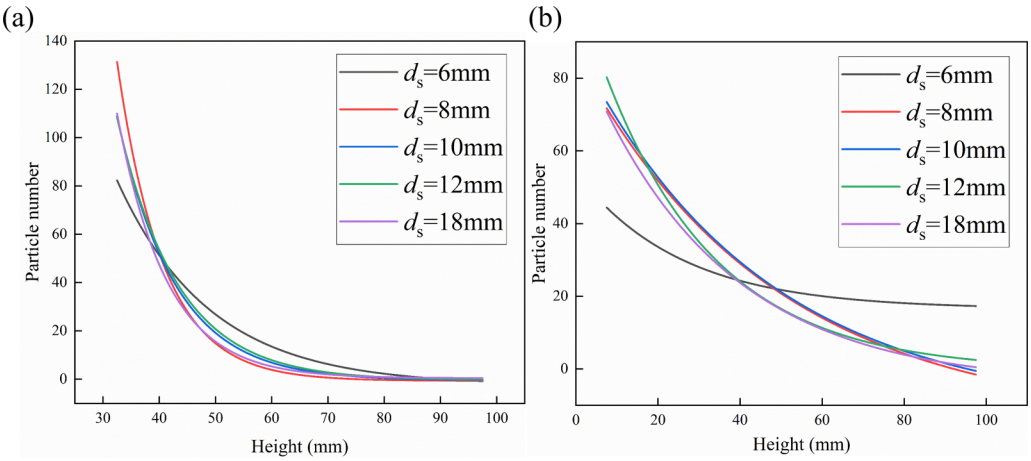

FIG. 12. Fitted curves of the numbers of the entrained particles at different heights for several orifice distances under the fixed air-intaking velocity ($v_g = 0.5\,\mathrm{m/s}$) at time (a) $t = 0.60$ and (b) $t = 1.0\,\mathrm{s}$.

the coalescence of two bubbles could carry more particles to a higher place. When time $t = 1.0\,\mathrm{s}$ [see Fig. 12(b)], this is more evident. Since near the top g-l surface only the particle number for $d_s = 6\,\mathrm{mm}$ is relatively large, while, the particle numbers for the other four curves are all close to zero.

The number of particle entrainment at a fixed time could be obtained by integrating the lines shown in Fig. 12. The particle percentages (ratio of the number of entrained particles to the total particle number) at different time are shown in Fig. 13. It is clear that the numbers of the entrained particles increase along with time continuously. In addition, according to this figure, it could be seen that the particle numbers for $d_s = 6$, 8, and 10 mm are larger than those for $d_s = 12$ and 18 mm. This means when the air-intaking velocity is fixed, choosing the proper distance between two orifices is necessary in order to obtain a large particle entrainment.

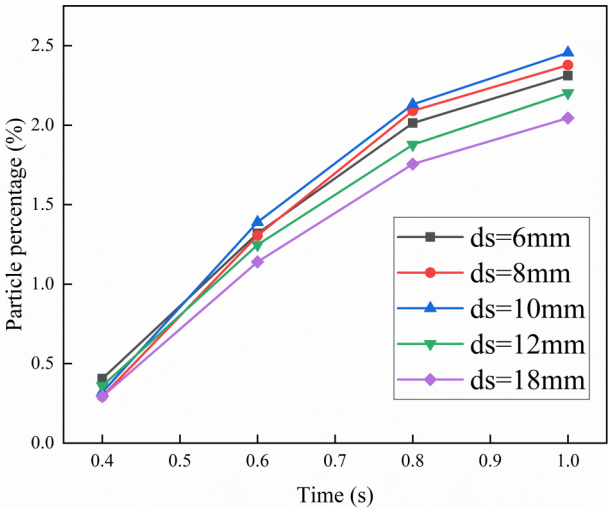

FIG. 13. Time evolution of the percentages of entrained particles by the two bubble queues for different orifice distances under the fixed air-intaking velocity ($v_g = 0.5\,\mathrm{m/s}$).

3. Particle entrainment for different orifice distances under different air-intaking velocities

Through the work in Sec. IV B 2, it could be seen that the orifice distance is important to the ability of particle entrainment of double bubbles when the air-intaking velocity is fixed to 0.5 m/s. It is natural to think that the change of the air-intaking velocity might affect the choosing of the proper orifice distance. In this section, different air-intaking velocities are taken, 0.6, 0.8, 1.0, 1.2, 1.4, and 1.6 m/s, and different orifice distances are also taken, 6, 8, 10, 12, 14, 16, and 18 mm.

After the calculation, the percentage of the entrained particles under different air-intaking velocities for several orifice distances at different time are shown in Fig. 14. According to Fig. 14(a), it could be seen that the ability of particle entrainment is the poorest for $d_s = 6$ mm when $v_g = 0.6$ m/s, and the bubbles have the stronger ability to carry particles for $d_s = 8$–14 mm when $v_g = 0.6$ m/s. According to Fig. 14(b), it could be seen that the ability of particle entrainment is the poorest for $d_s = 6$ mm when $v_g = 0.8$ m/s, and the bubbles have the stronger ability to carry particles for $d_s = 8$–18 mm when $v_g = 0.8$ m/s. According to Fig. 14(c), it could be seen that the ability of particle entrainment is the poorest for $d_s = 6$ mm when $v_g = 1.0$ m/s, and the bubbles have the stronger ability to carry particles for $d_s = 12$–18 mm when $v_g = 1.0$ m/s. According to Fig. 14(d), it could be seen that the ability of particle entrainment is the poorest for $d_s = 6$ and 8 mm when $v_g = 1.2$ m/s, and the bubbles have the stronger ability to carry particles for $d_s = 12$–18 mm when $v_g = 1.2$ m/s. According to Fig. 14(e), it could be seen that the ability of particle entrainment is the poorest for $d_s = 6$ and 8 mm when $v_g = 1.4$ m/s, and the bubbles have the stronger ability to carry particles for $d_s = 12$–18 mm when $v_g = 1.4$ m/s. According to Fig. 14(f), it could be seen that the ability of particle entrainment is the poorest for $d_s = 6$, 8, and 10 mm when $v_g = 1.6$ m/s, and the bubbles have the stronger ability to carry particles for $d_s = 12$–18 mm when $v_g = 1.6$ m/s. From these figures, it could be asserted that when the air-intaking velocity increases, the smaller orifice distance is not appropriate for the particle entrainment, and we should choose the larger orifice distance in order to enhance the particle entrainment.

For the investigated gas-liquid-solid system with double orifices, as the studying purpose is to find helpful results for the gas-liquid-solid fluidized bed, we could not only consider the numbers of the entrained particles; the distribution of the entrained particles is also important to consider. For example, it is not good that only particles in a very small domain are carried up even if the number is big. When particles are dispersed widely and sufficiently, the large contact area with the continuous phase is beneficial to the possible reaction in the fluidized system. In addition, when there are two orifices in the system, if the particles between these two orifices could not be carried up efficiently, this means that the common action of the two bubble queues from different orifices is weak and the orifice distance is too large, not the proper one. Thus, when selecting the best air-intaking velocity and the best orifice distance, we should not only focus on the particle numbers but also consider the even degree of the particle distribution. For this reason, the particle distributions in the x direction for different orifice distances and air-intaking velocities at a fixed time ($t = 1.0$ s) are shown in Fig. 15.

According to Fig. 15, it could be seen when the orifice distance is 18 mm there is an obvious valley between two peaks of the particle numbers. The two peaks corresponds to the two orifices. This situation is more like two independent orifices which intake air and trigger the particle entrainment separately. Although the number of entrained particles might be still large under some certain conditions, the orifice distance of 18 mm is regarded as a bad choice since the particles between these two orifices could be carried up efficiently under this air-intaking velocity. In addition, it would not be a good choice for the orifice distance either, if the entrained particles are too concentrated. When the orifice distance is too small relatively to the air-intaking velocity, the bubbles might coalesce before the bubble detachment from the container bottom, and the overall process could be approximately regarded as a single orifice. This explains the single sharp peak in Fig. 15. According to Fig. 15(a), it could be seen that the particle distribution with a high single peak is too narrow for $d_s = 6$–8 mm and the distribution is relatively even for $d_s = 12$ and 14 mm. It is anticipated that the best choice of the orifice distance is somewhere between 12 and 14 mm when

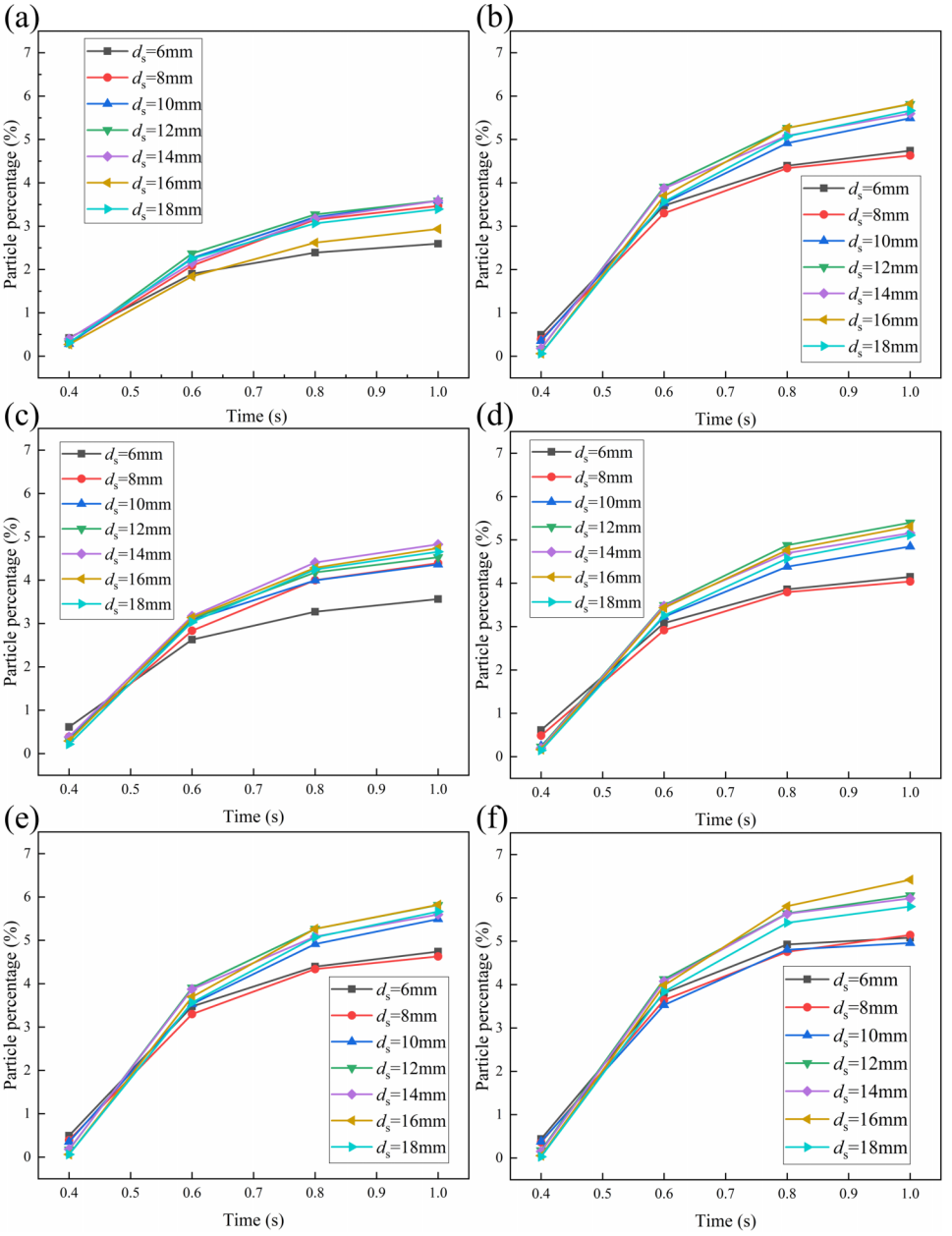

FIG. 14. Percentage of the entrained particles under different air-intaking velocities for several orifice distances at different time when particles are freely settling. (a) $v_g = 0.6$, (b) $v_g = 0.8$, (c) $v_g = 1.0$, (d) $v_g = 1.2$, (e) $v_g = 1.4$, and (f) $v_g = 1.6$ m/s.

the air-intaking velocity is 0.6 m/s. As for Fig. 15(b) when the air velocity is 0.8 m/s, combined with the result of Fig. 14(b), the orifice distance of a little less than 14 mm might be the proper one. Figure 15(c) when the air velocity is 1.0 m/s is similar to Fig. 15(b). According to Fig. 15(d), when the air-intaking velocity is 1.2 m/s, the best choice of the orifice distance might be a little larger than 14mm. Figure 15(e) when the air-intaking velocity is 1.4 m/s is similar to Fig. 15(d). According to Fig. 15(f), it could be seen that the distributions for $d_s = 14$ and 16 mm are quite well when the

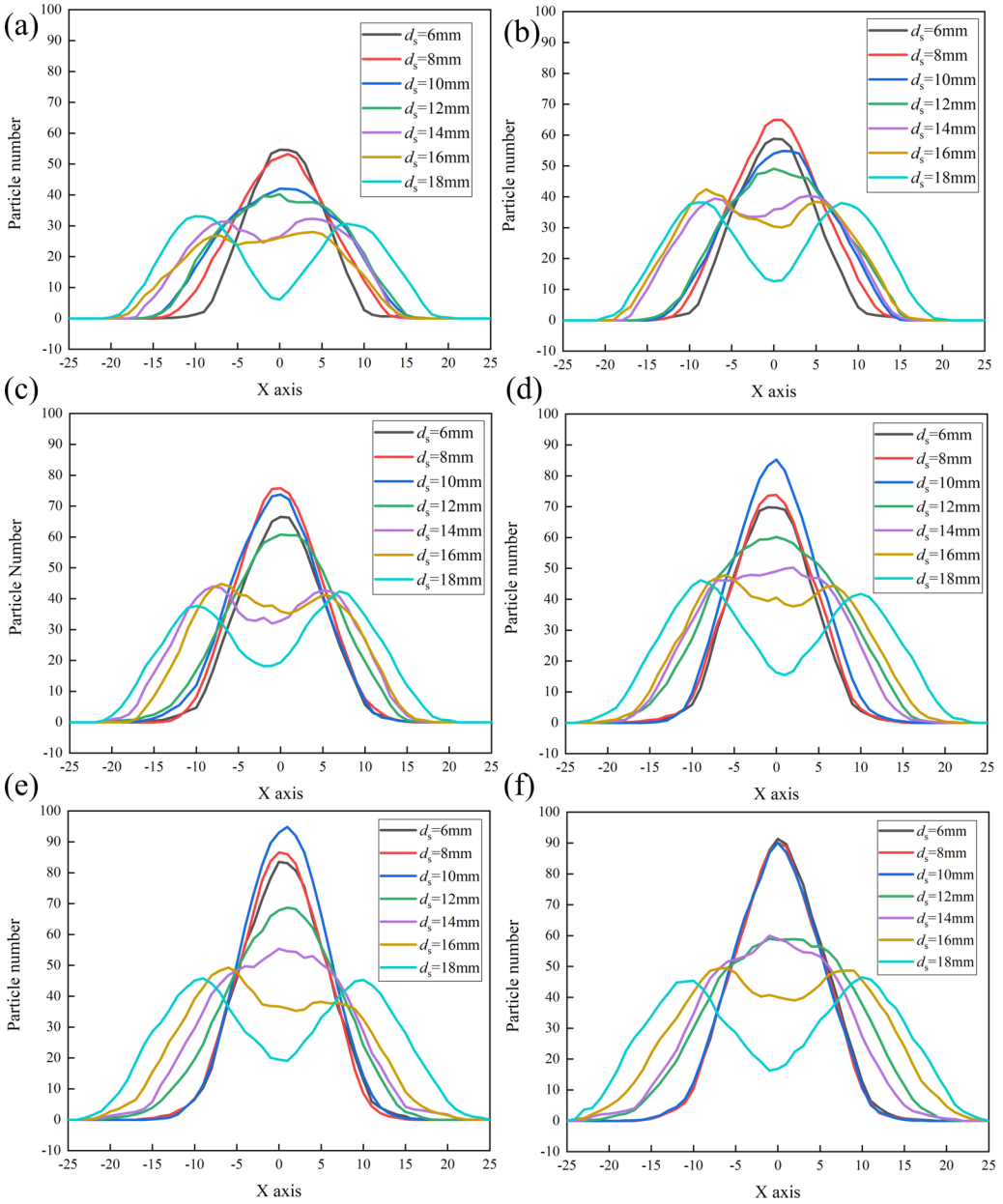

FIG. 15. Particle distributions in the x direction for different orifice distances and air-intaking velocities at a fixed time. (a) $v_g = 0.6$, (b) $v_g = 0.8$, (c) $v_g = 1.0$, (d) $v_g = 1.2$, (e) $v_g = 1.4$, and (f) $v_g = 1.6\,\mathrm{m/s}$.

air-intaking velocity is 1.6 m/s. Combined with the result in Fig. 14(f), the best choice of the orifice distance is somewhere between 14 and 16 mm. Totally, the trend is that the most suitable distance of two orifices for particle entrainment increases as the air-intaking velocity increases.

V. CONCLUSION

In this paper, VOF-DEM method is employed to calculate the formation and rising of double bubbles generated through two different orifices in a three-dimensional gas-liquid-solid flow system.

Volume of fluid method is used to capture the interface of bubbles, and discrete element model is used to track the movement of particles. A series of model verification is done in order to verify the accuracy and validation of VOF-DEM model.

The bubble formation and rising for two cases, when particles are laid at the container bottom (case I) and when particles are settling freely (case II), are studied carefully. Firstly, for case I, it could be seen that the coalescence of two bubbles from two different bubble queues and the deviation of two bubble queues from the vertical direction occur during the rising process. The main reasons for these phenomena are analyzed through the velocity vector diagrams, and they are caused by the water vortices and eddies between the two bubble queues and between the side wall and the bubble queues. In addition, the detachment time of the first bubble is less when there is a proper time difference of the start of the air intake of two different orifices than that when the start time of the air intake is the same for the two orifices. The main reason is that the time difference of the air intake start avoids the simultaneous expansion and contraction of the two first bubbles. When the earlier first bubble expands, the later first bubble almost has not started; when the earlier one contracts, the later one expands, which enhances the detachment of the first bubble. Secondly, by comparing case I and case II, it is disclosed that the free settlement of particles could prevent bubbles from coalescence and weaken the deviation of the bubble queues. As the particle settlement will enhance the upward movement of water at the lower half of the container due to the volume conservation, the relatively stronger upwards and downwards currents of water will enhance the upward movement of the bubbles and hinder the left or right shift of the bubbles. Finally, by counting the number of entrained particles, the suitable distance of two orifices under different air-intake velocities are analyzed in order to realize a better particle entrainment. It could be seen that the particle entrainment of two relatively independent orifices is obviously not satisfying since the particles between these two orifices could not be carried up efficiently. Meanwhile, the particle entrainment of two very close orifices is also not satisfactory since only particles within a limited domain are carried up. Thus, those cases with two orifices of suitable distances, for which there is a wider and even distribution of entrained particles, are the promising ones. Furthermore, it is also disclosed that the suitable distance of two orifices increases when the air-intaking velocity increases. These results might be useful in the design and deep understanding of the hydrodynamics of the gas-liquid-solid fluidized system.

ACKNOWLEDGMENTS

This work was supported by National Natural Science Foundation of China (Grant No. 22078229) and National Key R&D Program of China (Grant No. 2019YFC1905805).

[1] M. R. Rampure, V. V. Buwa, and V. V. Ranade, Modelling of gas-liquid/gas-liquid-solid flows in bubble columns: Experiments and CFD simulations, Can. J. Chem. Eng. **81**, 692 (2003).

[2] J. Wen, P. Lei, and L. Huang, Modeling and simulation of gas-liquid-solid three-phase fluidization, Chem. Eng. Commun. **192**, 941 (2007).

[3] M. Abbasi, J. R. Grace, R. Sotude-Gharebagh, R. Zarghami, and N. Mostoufi, Numerical comparison of gas-liquid bubble columns and gas-solid fluidized beds, Can. J. Chem. Eng. **93**, 1838 (2015).

[4] M. Liu and Z. Hu, Studies on the hydrodynamics of chaotic bubbling in a gas-liquid bubble column with a single nozzle, Chem. Eng. Technol. **27**, 537 (2004).

[5] A. Muhlbauer, M. W. Hlawitschka, and H. J. Bart, Models for the numerical simulation of bubble columns: A review, Chem. Ing. Tech. **91**, 1747 (2019).

[6] I. Khan, M. J. Wang, Y. P. Zhang, W. X. Tian, G. H. Su, and Q. Z. Su, Two-phase bubbly flow simulation using CFD method: A review of models for interfacial forces, Prog. Nucl. Energ. **125**, 103360 (2020).

[7] X. Wang and X. D. Sun, Three-dimensional simulations of air–water bubbly flows, Int. J. Multiphase Flow **36**, 882 (2010).

[8] Q. Chen, K. Polila, Y. F. Rao, R. Boeden, and S. K. Yang, Assessment of CFD for unheated gas-liquid flows with high void fraction, Nucl. Eng. Des. **341**, 346 (2019).
[9] R. Panneerselvam, S. Savithri, and G. D. Surender, CFD simulation of hydrodynamics of gas-liquid-solid fluidised bed reactor, Chem. Eng. Sci. **64**, 1119 (2009).
[10] K. Kiared, F. Larachi, J Chaouki, and C. Guy, Mean and turbulent particle velocity in the fully developed region of a three-phase fluidized bed, Chem. Eng. Technol. **22**, 683 (1999).
[11] Y. H. Yu and S. D. Kim, Bubble characteristics in the radial direction of three-phase fluidized beds, AIChE J. **34**, 2069 (1988).
[12] Y. H. Yu and S. D. Kim, Bubble-wake model for radial velocity profiles of liquid and solid phases in three-phase fluidized beds, Ind. Eng. Chem. Res. **40**, 4463 (2001).
[13] E. Delnoij, J. A. M. Kuipers, and W. P. M. V. Swaaij, Computational fluid dynamics applied to gas-liquid contactors, Chem. Eng. Sci. **52**, 3623 (1997).
[14] D. Darmana, N. G. Deen, and J. A. M. Kuipers, Parallelization of an Euler–Lagrange model using mixed domain decomposition and a mirror domain technique: Application to dispersed gas–liquid two-phase flow, J. Comput. Phys. **220**, 216 (2006).
[15] X. Zhang and G. Ahmadi, Eulerian-Lagrangian simulations of liquid–gas–solid flows in three-phase slurry reactors, Chem. Eng. Sci. **60**, 5089 (2005).
[16] P. A. Cundall and O. D. L. Strack, A discrete numerical model for granular assemblies, Géotechnique **30**, 331 (1980).
[17] J. Ai, J. F. Chen, J. M. Rotter, and J. Y. Ooi, Assessment of rolling resistance models in discrete element simulations, Powder Technol. **206**, 269 (2011).
[18] R. Namdarkedenji, K. Hashemnia, and H. Emdad, Effect of flow pulsation on fluidization degree of gas-solid fluidized beds by using coupled CFD-DEM, Adv. Powder Technol. **29**, 3527 (2018).
[19] D. Gueyffier, J. Li, A. Nadim, R. Scardovelli, and S. Zaleski, Volume-of-fluid interface tracking with smoothed surface stress methods for three-dimensional flows, J. Comput. Phys. **152**, 423 (1999).
[20] J. Zhang, L. Yong, and L. S. Fan, Discrete phase simulation of gas-liquid-solid fluidization systems: Single bubble rising behavior, Powder Technol. **113**, 310 (2000).
[21] Y. G. Xu, M. Y. Liu, and C. Tang, Three-dimensional CFD-VOF-DPM simulations of effects of low-holdup particles on single-nozzle bubbling behavior in gas-liquid-solid systems, Chem. Eng. J. **222**, 292 (2013).
[22] D. F. Rivas, L. Stricker, A. G. Zijlstra, H. J. G. E. Gardeniers, D. Lohse, and A. Prosperetti, Ultrasound artificially nucleated bubbles and their sonochemical radical production, Ultrason. Sonochem. **20**, 510 (2013).
[23] D. Bhaga and M. E. Weber, Bubbles in viscous liquids: Shapes, wakes and velocities, J. Fluid Mech. **105**, 61 (2006).
[24] W. L. Shew and J. F. Pinton, Dynamical Model of Bubble Path Instability, Phys. Rev. Lett. **97**, 144508 (2006).
[25] H. Wang, Z. Y. Zhang, Y. M. Yang, and H. S. Zhang, Viscosity effects on the behavior of a rising bubble, J. Hydrodyn. **22**, 81 (2010).
[26] Y. Huang, P. Z. Gao, P. Xu, C. Q. Wang, and X. L. Qian, Visualization study on dynamic behaviors of horizontal arranged bubbles, J. Chem. Eng. Chin. Uni. **33**, 557 (2019).
[27] J. Zhang, M. Y. Liu, Y. G. Xu, and C. Tang, Three-dimensional volume of fluid simulations on bubble formation and dynamics in bubble columns, Chem. Eng. Sci. **73**, 55 (2012).
[28] L. Wu, M. Gong, and J. Wang, Development of a DEM–VOF model for the turbulent free-surface flows with particles and its application to stirred mixing system, Ind. Eng. Chem. Res. **57**, 1714 (2018).
[29] N. Zhao, B. Wang, Q. Q. Kang, and J. T. Wang, Effects of settling particles on the bubble formation in a gas-liquid-solid flow system studied through a coupled numerical method, Phys. Rev. Fluids **5**, 033602 (2020).
[30] S. K. Garg and J. W. Pritchett, Dynamics of gas-fluidized beds, J. Appl. Phys. **46**. 4493 (1975).
[31] J. U. Brackbill, D. B. Kothe, and C. Zemach, A continuum method for modeling surface tension, J. Comput. Phys. **100**, 335 (1992).

[32] S. Balachandar and J. K. Eaton, Turbulent dispersed multiphase flow, Annu. Rev. Fluid Mech. **42**, 111 (2010).
[33] Y. Tsuji, T. Kawaguchi, and T. Tanaka, Discrete particle simulation of two-dimensional fluidized bed, Powder Technol. **77**, 79 (1993).
[34] R. D. Mindlin and H. Deresiewicz, Elastic spheres in contact under varying oblique forces, J. Appl. Mech. **20**, 327 (1953).
[35] J. Ding and D. Gidaspow, A bubbling fluidization model using kinetic theory of granular flow, AIChE J. **36**, 523 (1990).
[36] M. Robinson, M. Ramaioli, and S. Luding, Fluid–particle flow simulations using two-way-coupled mesoscale SPH–DEM and validation, Int. J. Multiphase Flow **59**, 121 (2014).
[37] J. Zhao and T. Shan, Coupled CFD–DEM simulation of fluid–particle interaction in geomechanics, Powder Technol. **239**, 248 (2013).
[38] X. S. Sun and M. Sakai, Three-dimensional simulation of gas–solid–liquid flows using the DEM–VOF method, Chem. Eng. Sci. **134**, 531 (2015).
[39] G. Pozzetti and B. Peters, A multiscale DEM-VOF method for the simulation of three-phase flows, Int. J. Multiphase Flow **99**, 186 (2018).
[40] See Supplemental Material at http://link.aps.org/supplemental/10.1103/PhysRevFluids.7.024303 for supplementary video.
[41] H. Pan, X. Z. Chen, X. F. Liang, L. T. Zhu, and Z. H. Luo, CFD simulations of gas-liquid-solid flow in fluidized bed reactors – A review, Powder Technol. **299**, 235 (2016).